processes

MDPI

Article

Numerical Study on Primary Breakup of Disturbed Liquid Jet Sprays Using a VOF Model and LES Method

Zhenming Liu [1,*], Ziming Li [1], Jingbin Liu [1], Jiechang Wu [1], Yusong Yu [2] and Jiawei Ding [3]

[1] College of Power Engineering, Naval University of Engineering, Wuhan 430033, China; zmingli_issac@163.com (Z.L.); bin_lj@126.com (J.L.); wujiechang1234@163.com (J.W.)
[2] Hydrogen Energy and Space Propulsion Laboratory (HESPL), School of Mechanical, Electronic and Control Engineering, Beijing Jiaotong University, Beijing 100044, China; ysyu@bjtu.edu.cn
[3] Xi'an Aerospace Propulsion Test Technique Institute, Xi'an 710100, China; dingjw163@163.com
* Correspondence: liuzhenmingyk@163.com

Abstract: In this study, the primary breakup of a high-speed diesel jet is investigated using a CFD methodology that combines an LES model with a VOF technique for free surface capture. Inner-nozzle turbulence and cavitation are simplified as the sinusoidal radial velocity with a given amplitude and frequency. The ligament and droplet formation process are captured, the liquid jet is disturbed by the radial velocity, and umbrella-shaped crests are created. Meanwhile, ligaments are formed from the edges of crests because of shear stress and surface tension. We investigate the effect on the characteristics of the surface wave and the liquid structure of different disturbance frequencies and amplitudes. The variation in the disturbance amplitude and frequency facilitates the formation of a variety of liquid structures, such as waves, upstream/downstream-directed bells, and droplet chains. Increasing the disturbance frequency reduces the growth rate of the surface waves of the liquid jet. With an increase in disturbance amplitude, the amplitude of surface waves evidently increases. Furthermore, as the disturbance frequency and amplitude increase, the thickness and Weber number of the radial liquid sheet decrease, and this causes the ligament diameter of the primary breakup to become small. Finally, the primary breakup time is investigated, and the time scale of the liquid jet primary breakup decreases as the disturbance amplitude increases, which indicates that an increase in the disturbance amplitude promotes the atomization of a disturbed liquid jet.

Keywords: volume of fluid (VOF); large-eddy simulation (LES); spray; primary breakup; surface wave; ligament

Citation: Liu, Z.; Li, Z.; Liu, J.; Wu, J.; Yu, Y.; Ding, J. Numerical Study on Primary Breakup of Disturbed Liquid Jet Sprays Using a VOF Model and LES Method. *Processes* **2022**, *10*, 1148. https://doi.org/10.3390/pr10061148

Academic Editor: Jiangping Tian

Received: 6 May 2022
Accepted: 3 June 2022
Published: 8 June 2022

1. Introduction

Liquid atomization is an important process in direct injection diesel engines. The quality of spray atomization directly affects fuel combustion, which consequently determines engine performance, including parameters such as the fuel consumption rate and exhaust gas cleanness. Liquid atomization is a complicated phenomenon with mechanisms that have yet to be fully explored; comprehensive studies are therefore needed to facilitate a good understanding of this process [1].

In high-pressure injection diesel engines, liquid jet atomization is a complicated phenomenon, which is influenced by many factors [2,3]. Normally, the breakup of the liquid jet does not occur in a single mechanism. The process involves complicated flow mechanisms, including nozzle internal turbulence flow [4–6], cavitation [7–11], and aerodynamic effects [12–14]. In the liquid core region at the nozzle exit, liquid surface instability occurs because of disturbance and aerodynamic interaction. Ligaments and droplets are generated from the liquid core in a process that is called primary breakup. Ligament and large droplets break up into small droplets because of aerodynamic interaction, and this process is called secondary breakup. The quality of spray atomization is considerably dependent on the primary breakup.

Numerous studies have focused on the mechanism of aerodynamic interaction. However, primary breakup is facilitated by complicated mechanisms. Schweitzer [15] concluded that the turbulence inside injector nozzles provides a radial velocity at the exit of the nozzles, and this velocity is an important disturbance source for spray atomization. Bague [5] highlighted that turbulent kinetic energy can provide sufficient energy, and ligaments are generated at the nozzle exit. Bergwerk [16] attributed primary breakup to the pressure disturbance caused by cavitation inside nozzles. Chaves [17] and Soteriou [18] investigated the characteristics of nozzle flow, particularly the cavitation phenomenon, inside a transparent injector and emphasized that cavitation bubbles cause a strong disturbance at the nozzle exit. This disturbance facilitates atomization near the nozzle exit. The flow transition in the low-lift zone and the cavitation change in the high-lift stable zone cause a transformation in the form of pressure fluctuations, which change the near-field spray dynamics [19]

The structure and physics of a disturbed liquid jet have been extensively studied. McCormack [20] analyzed the formation of a disc structure of a disturbed liquid jet. Chaves et al. [21] investigated the disintegration of a liquid jet disturbed by sinusoidal radial velocity and reported different spray structures at various disturbance frequencies and amplitudes. Geschner et al. [22] plotted a nondimensional map for the spray structures of a disturbed liquid jet. Srinivasan et al. [23,24] applied the volume of fluid (VOF) methodology to a modulated liquid jet, and simulations exhibited the behavior of a modulated liquid jet under a given set of nondimensional parameters. In recent work by Hwang et al. [25], strong amplification of the interface perturbation by a multiphase Orr mechanism was shown to be a possible pathway to distort the liquid jet. Chenling Zhou et al. [26] analyzed the evolution process of jet surface waves at different disturbance frequencies ranging from 0−3000 kHz based on the VOF interface capturing method. In this study, the effect of disturbance amplitude is not considered.

Experimentally investigating the mechanism of primary breakup is difficult because the study region is small, and the liquid core is surrounded by dense droplets. Linne et al. [27] obtained 2D images of the near field of a diesel spray, but primary droplets were smaller than the resolution limit. Blaisot and Yon [28] investigated the distribution of droplet size with an image analysis technique. Wang et al. [29] used velocity measurements to examine the spray structure of a dense spray near the nozzle. To investigate the effect of internal flow on the primary atomization, a high-magnification diffused backlight imaging technique was used by means of a high-speed light-emitting diode and a long-distance microscope [30]. The results show that higher turbulence at the nozzle outlet induces higher variability in the spray shape. Research that investigates the complete mechanisms of liquid atomization is ongoing.

In numerical simulations, combining multiphase VOF and direct numerical simulation (DNS) or large-eddy simulation (LES) methodologies [31] is a powerful tool to study the breakup process of the liquid jet. In DNS, the details of turbulent flow fields in liquid and gas, as well as the topology of interfaces, are directly calculated by numerical calculations of Navier–Stokes equations [32]. However, the small length and time scales, as well as the high velocity in high-speed liquid jets, require submicron computational elements and picosecond time steps. The computation requirement is large, even on a parallel computer system. An alternative approach is LES, which aims only to resolve eddies that are large enough to contain information on the problem geometry and most of the turbulent energy. It is a powerful tool to investigate the physics of primary breakup.

Computational performance has been steadily increasing, and parallel computing has been widely applied. Considerable efforts have been exerted to calculate the liquid jet atomization process and to determine the physical mechanisms of liquid atomization. Menard et al. [33] investigated the atomization process of a liquid jet injected into still gas with the use of coupled level set/VOF/ghost methods, but the grid resolution was coarse for the selected Reynolds and Weber numbers, and the ligaments and droplets did not exhibit smooth shapes or wave dynamics. Desjardins [34] used a conservative level set method to compute the primary atomization of a straight liquid jet. Villiers [35]

applied the LES-VOF method to a round jet and investigated the atomization process under the influence of the nozzle flow. Pai et al. [36] simulated the primary breakup of cross flows, and the detail of atomization was well resolved with 100 million grids. Herrmann [37–39] discussed the effect of grid resolution on droplet size distribution. Shinjo and Umemura [9,10] characterized the liquid surface instability that results in primary atomization with the use of a detailed numerical simulation. K. Liu et al. [40] simulated the process of atomization of a liquid jet by coupling a two-phase large-eddy simulation and Lagrange spray simulation. Cosan Daskiran et al. [41] also found that the energy dissipation rate was higher, and its peak values were found to be closer to the jet centerline with the pipe orifice using the LES-VOF method.

In a high-pressure injection diesel engine, the speed of a liquid jet can exceed 400 m/s. Compared with a low-speed liquid jet, inner-nozzle turbulence and cavitation are key factors that affect the atomization process, such that the physical mechanism of primary breakup becomes more complicated. Therefore, investigating the atomization characteristics and breakup mechanism of a disturbed high-speed liquid jet is important. In doing so, we simplify the inner-nozzle turbulence and cavitation effects as the sinusoidal radial velocity, and the VOF method and LES model are used to compute the atomization process of a disturbed liquid jet.

2. Numerical Methods

2.1. Governing Equations

The mathematical representation describes the simultaneous flow of two immiscible fluids, each having a constant viscosity and including surface tension. The flow is considered to be an isothermal Newtonian flow. The mass continuity and momentum equations are as follows:

$$\frac{\partial \overline{u}_i}{\partial x_i} = 0 \tag{1}$$

$$\rho \frac{\partial \overline{u}_i}{\partial t} + \rho \frac{\partial \left(\overline{u}_i \overline{u}_j\right)}{\partial x_j} = -\frac{\partial \overline{p}}{\partial x_i} + \frac{\partial}{\partial x_j}\left(\mu \frac{\partial \overline{u}_i}{\partial x_j}\right) + \overline{F}_i + \overline{G}_i \tag{2}$$

where the upper overbar denotes filtered quantities; i.e., they are the ones directly computed during the LES simulation.

2.2. Subgrid Turbulence Model

SGS stress can be approximated by the SGS model. The Smargorinsky model [42] is the most widely used model and can be written as Equation (3). It is based on the eddy viscosity assumption, which assumes a linear relationship between the SGS stress and the resolved rate of the strain tensor to model the anisotropic residual-stress tensor.

$$\overline{t}_{ij} = -2v_t \overline{S}_{ij} \tag{3}$$

where $v_t = C_S \Delta^2 \left(2\overline{S}_{ij}\overline{S}_{ij}\right)^{1/2}$, $\overline{S}_{ij} = \frac{1}{2}\left(\frac{\partial \overline{u}_i}{\partial x_j} + \frac{\partial \overline{u}_j}{\partial x_i}\right)$ is the mean strain rate tensor, and the constant Cs is 0.18.

2.3. VOF Scheme

The interface between phases is simultaneously computed with the VOF method [43], which employs the volume fraction of one of the phases as an indicator function to mark the different fluids. The liquid volume fraction γ is defined as

$$\gamma = \frac{\iiint\limits_{\text{cell}} \gamma(x,y,z)dxdydz}{\iiint\limits_{\text{cell}} dxdydz} \tag{4}$$

The flow field can be divided into three regions, as follows:

When $\gamma = 0$, the computational cell is filled with gas;
When $\gamma = 1$, the computational cell is filled with liquid;
When $0 < \gamma < 1$, there is a fluid interface in the computational cell.

The indicator function associated with a particular fluid is propagated with it as a Lagrangian invariant, which obeys a transport equation of the form

$$\frac{\partial \gamma}{\partial t} + \nabla \cdot (\overline{u}\gamma) = 0 \tag{5}$$

From the definitions of the indicator function, the local density and viscosity in a computational cell are given in terms of the liquid volume fraction by

$$\rho = \gamma\rho_l + (1 - \gamma)\rho_g \tag{6}$$

$$\mu = \gamma\mu_l + (1 - \gamma)\mu_g \tag{7}$$

where subscripts l and g represent the liquid and gas phases, respectively. The interface is treated as a transitional zone, such that its exact shape and location are not explicitly known. The surface tension force in Equation (2) cannot be directly calculated. Brackbill et al. [44] addressed this problem with the continuum surface force (CSF) model. Employing the CSF model, we represent the surface tension force as a continuous volumetric force:

$$F = \int_{s(t)} \sigma k' \overline{n}' \delta\left(\vec{x} - \vec{x}'\right) dS \approx \sigma k \nabla \gamma \tag{8}$$

where the curvature of the interface k is given by

$$k = \nabla \cdot \left(\frac{\nabla \gamma}{|\nabla \gamma|}\right) \tag{9}$$

2.4. Numerical Methodology

The employed transient multiphase solver of OpenFOAM, a free, open source software for CFD from the OpenFOAM Foundation in Delaware USA, utilizes a cell-center-based finite volume method and provides a comprehensive range of discretization schemes that can be selected for each term in the equations being solved. The Crank–Nicholson method with second-order accuracy was used for the time discretion of the governing equations. For general field interpolations, a linear form of the central differencing scheme was applied. Convective fluxes were discretized with the Gauss linear scheme. Pressure velocity coupling was addressed with the pressure implicit split operator (PISO) algorithm [45]. An interface compression scheme was used to obtain a sharp interface. The "snGradSchemes", a standard surface-normal gradient scheme in OpenFOAM, sets the discretization for calculating the normal vector to the surface. In addition, OpenFOAM uses an additional counter-gradient convection-based term that compresses the interface while maintaining boundedness and conservativeness. The fluxes were limited and corrected using the MULES algorithm.

3. Simulation Setup and Boundary Conditions

Figure 1 shows the major computational system with the relevant boundary conditions expected in the present calculation. The simulations focus on the region downstream of a 0.2 mm diameter nozzle that releases a fully developed turbulent liquid flow into a dense, initially stationary gas. Boundary conditions include the pressure condition (atmosphere), no-slip wall condition (wall), and mass flow condition (inlet). The flow conditions are listed in Table 1 according to the experiment conducted by Blessing et al. [46]. The liquid is diesel fuel, and the gas is air at a pressure and temperature of approximately 1 bar, as summarized in Table 1. The inlet velocity distribution was set to a parabolic profile with the decrease in radial distance to the central point, and the maximum value U_{max} = 336 m/s occurs at the central point of the inlet boundary face.

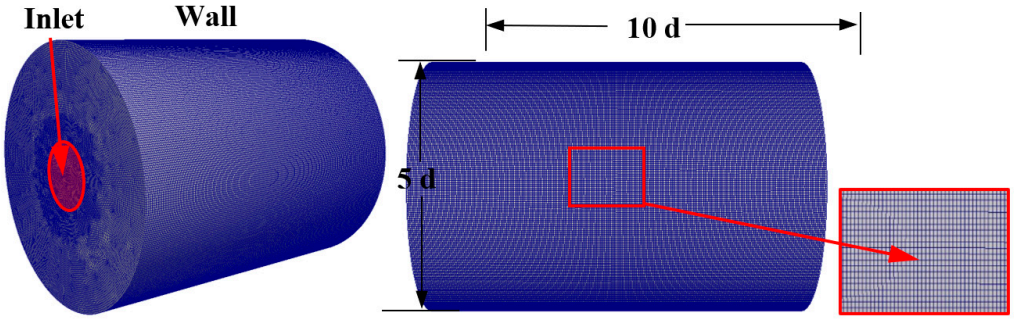

Figure 1. Calculation domain, grids, and boundary conditions.

Table 1. Flow conditions.

Parameters	Value
Nozzle diameter (mm)	0.2
Ambient pressure (MPa)	0.1
Ambient temperature (K)	298.15
Gas density (kg/m^3)	1.29
Liquid density (kg/m^3)	840
Gas dynamic viscosity (Pa·s)	1.79×10^{-5}
Liquid kinematic viscosity (m^2/s)	2.87×10^{-6}
Surface tension coefficient (N/m)	0.026
Injection pressure (MPa)	80
Injecting velocity of liquid jet (m/s)	336

The average grid resolution and the number of cells are 12 μm and 0.84 million, respectively. The average grid size on the inlet boundary face, i.e., the nozzle exit section, is about 4 μm, and the cell number on the inlet boundary face is 1652. An adaptive mesh refinement technique was used at the interface of the liquid and gas. Therefore, the predicted structure of the spray and the droplet distribution are similar to those predicted with the use of a fine mesh. The minimum mesh size is 3 μm [47], and the maximum number of cells is limited to 10 million to avoid memory overflow. The simulation was run in parallel using multiple threads on a Dell PowerEdge server with dual CPU, Intel Xeon E6126 (2.6 GHz), and 256 Gb RAM. The module named dynamicRefineFvMesh in OpenFOAM was used to realize the function of adaptive mesh refinement. In the present study, the original interFoam solver was modified to interDyMFoam after coupling with the dynamicRefineFvMesh module. The dynamicRefineFvMesh module does not morph the mesh shape. Instead, it performs topological refinements to the mesh based on the value of specified fields. We define the refinement threshold relative to the minimum (0.01) and maximum (0.09) values of alpha.liquid (i.e., the liquid volume fraction) as the refined field, which is the liquid–gas surface. The detailed settings of dynamicFvMesh are as follows:

```
dynamicFvMesh dynamicRefineFvMesh;
dynamicRefineFvMeshCoeffs
{
refineInterval 20;
field alpha.liquid;
lowerRefineLevel 0.01;
upperRefineLevel 0.99;
unrefineLevel 30;
nBufferLayers 1;
maxRefinement 2;
maxCells 20,000,000;
correctFluxes
(
```

```
(phi U)
);
dumpLevel true;
}
```

The example of adaptive mesh refinement is shown in Figure 2. The maxRefinement parameter determines the maximum number of times that a cell can be cut. In this study, with maxRefinement 2, a hexahedral type of cell can be cut at most twice, thus giving rise to $2^3 \times 2^3$ (64 cells). The maxCells parameter limits the maximum number of cells in the model.

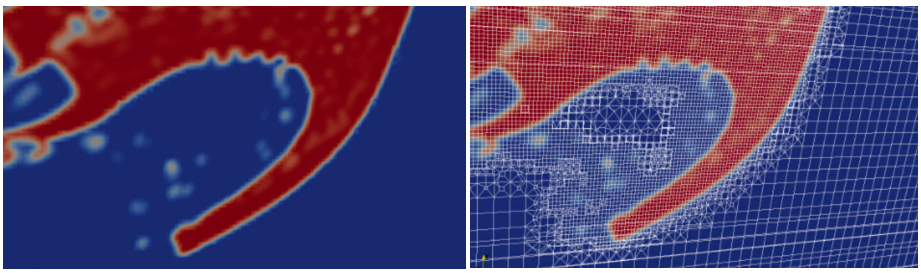

Figure 2. Adaptive mesh refinement of the liquid jet.

A grid independence analysis was carried out using four mesh resolutions: very coarse, coarse, medium, and fine grid (See Table 2). The same settings of the dynamicFvMesh were used for all cases. The minimum grid size can be refined down to 3 µm and 1.5 µm in the primary atomization zone for the medium and fine mesh cases, respectively.

Table 2. Summary of grids and computational parameters. Total calculation time is 200 µs.

Case	Initial Average Grid Size, µm	Cell Count	Time Step, ns	CPU (Core Count)	Wall Clock Time, h	Final Average Grid Size, µm
Very coarse	40	0.14×10^6	$0.5 \leq \Delta t \leq 2$	72	35	18.9
Coarse	20	0.36×10^6	$0.5 \leq \Delta t \leq 2$	72	64	9.7
Medium	12	0.84×10^6	$0.5 \leq \Delta t \leq 2$	72	120	5.6
Fine	6	2.35×10^6	$0.5 \leq \Delta t \leq 2$	72	282	2.8

Mass-averaged fluid velocities in the overall domain at 100 µs for the different cell counts (i.e., different grid sizes) are shown in Figure 3. The relative derivations, which were calculated based on the results of the fine mesh, between the medium and coarse meshes were in the order of 6.18%, while for the fine and medium meshes, it was 0.77%. To reduce computation consumption, the medium mesh was considered appropriate for the present study.

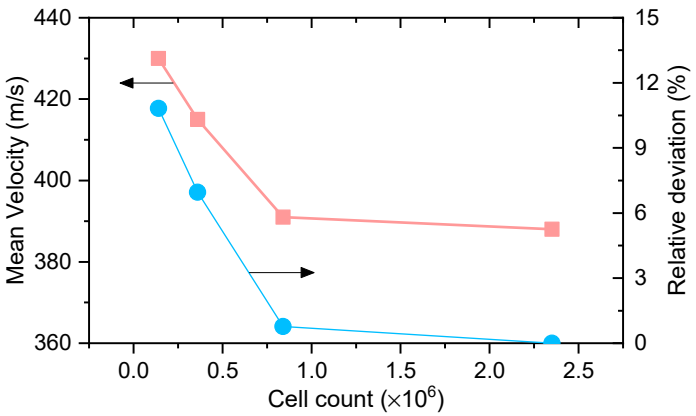

Figure 3. Comparison of mass-averaged velocities and relative deviations for different cell counts in the entire computational domain.

Disturbance at the Nozzle Exit

The flow inside the nozzle is cavitating and turbulent. Therefore, the fluctuating kinetic energy provides a fluctuating velocity at the nozzle exit. The disturbance at the nozzle exit is simplified as the transient radial velocity U_{rad} with a given amplitude $U_{rad,max}$, i.e., the maximum radial velocity, and frequency:

$$U_{rad} = U_{rad,max} sin(2\pi f \cdot t) \tag{10}$$

The amplitude and frequency of the disturbance vary according to the study requirements. Martinez et al. [35] stated that the maximum radial velocity of the liquid jet at the nozzle exit is given by

$$U_{rad,max} = \sqrt{3/2k_{tot}} \tag{11}$$

The total fluctuating kinetic energy k_{tot} is the sum of the turbulent kinetic energy and the energy provided by cavitation k_{cav}. Here, we assumed that the mainstream remains unchanged while the turbulence and cavitation in the nozzle change. The disturbance velocity was decomposed into x and y components that are perpendicular to jet velocity. According to the results by Martinez et al. [48], the radial velocity of liquid flow at the nozzle exit was calculated using Equation (11). The turbulent kinetic and cavitation energy of the internal flow in the nozzle was calculated (refer to [49–51]).

For the flow conditions in this study, the maximum radial velocity $U_{rad,max}$ is about 50 m/s. An overview of the simulation cases performed is shown in Figure 4. Twenty-eight cases were calculated to study the primary breakup of disturbed liquid jet sprays. The simulations cover a wide range of disturbance amplitudes and frequencies. The disturbance amplitude varies from 50 m/s to 200 m/s, whereas the disturbance frequency varies from 3000 kHz to 9000 kHz. The Strouhal number (Sr) and the nondimensional disturbance amplitude ε are calculated based on Equations (12) and (13) [21].

$$Sr = \frac{\pi D f}{U_{axial}} \tag{12}$$

$$\varepsilon = \frac{U_{rad,max}}{U_{axial}} \tag{13}$$

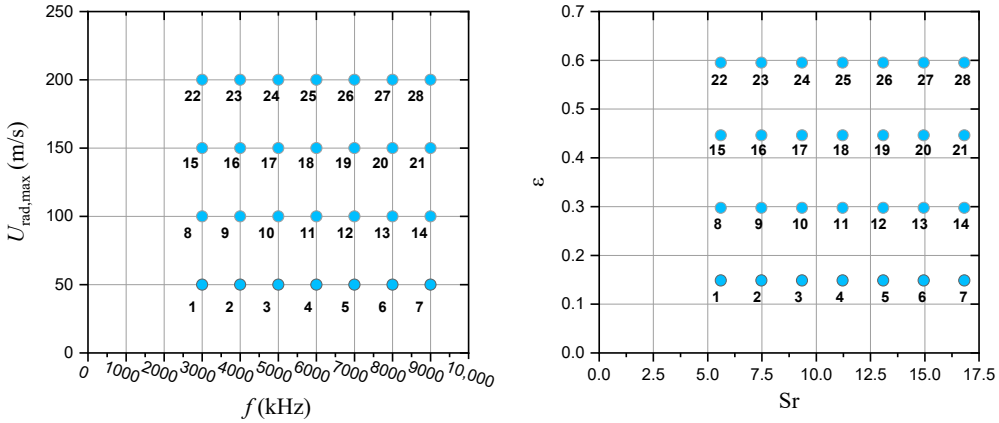

Figure 4. Simulation cases based on the disturbance amplitude and frequency (**left**), and Strouhal number (Sr) and the nondimensional disturbance amplitude ε (**right**).

4. Results and Discussion

4.1. Structure of Disturbed Liquid Jet Sprays

Figure 5 shows four different types of liquid structures. For (a), Sr = 5.6, ε = 0.15, and surface waves occur on the liquid jet surface. The surface wave's amplitude increases along the downstream direction and forms a relatively smooth disc-like liquid sheet. (b) Sr = 5.6,

ε = 0.30, and the disc-like structure becomes larger and disturbed. Lots of fragments separate from the periphery of sheets. (c) Sr = 7.5, ε = 0.45, and more fragments are generated at the rim of the liquid sheets, and the spray cone angle significantly increases. (d) Sr = 16.8, ε = 0.60, and the fragment size is more uniform and smaller. There is a slight decrease in the spray cone angle due to the lower penetration kinetic energy of the fine fragments.

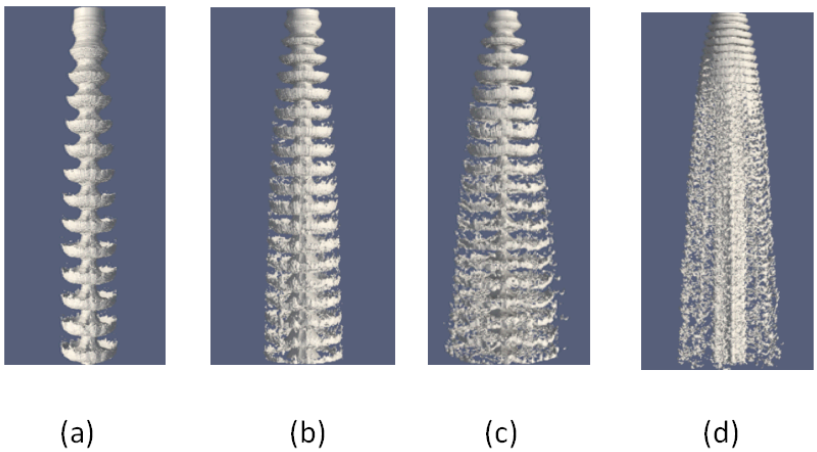

Figure 5. Generation of waves, discs, downstream-directed bells, and droplet chains. (**a**) Sr = 5.6, ε = 0.15; (**b**) Sr = 5.6, ε = 0.30; (**c**) Sr = 7.5, ε = 0.45; (**d**) Sr = 16.8, ε = 0.60.

To validate the results of the present simulations, we compared the simulation result with that of the experiment by Blessing et al. [33] (Figure 6). According to Blessing's experiment [46], the fuel injection and ambient pressures were set to 80 MPa and 0.1 MPa. The conical shape factor K and the diameter and length of the nozzle were 0.0, 0.2 mm, and 1.0 mm, respectively. We estimated the turbulence and cavitation kinetic energy of the internal flow using Huh's model based on the mean flow velocity and nozzle configuration parameters (nozzle length and diameter). As shown in Figure 6, the simulation spray angles (approx. 14.5°) were approximately equal to the experimental results under three conditions, as follows: Sr = 5.61 and ε = 0.15, Sr = 11.21 and ε = 0.45, and Sr = 5.61 and ε = 0.30; these values represent the structures of droplet chains, downstream-directed bells, and discs, respectively. To quantitatively validate which condition's simulation results are closer to reality, we compared the overall simulated mean droplet size with Jian Gao's experiment [52]. He carried out the spray experiment with similar conditions. In this study, the overall simulated mean droplet sizes for the values of Sr 14.95, 11.21, and 5.61 at 200 µs are 14.2 µm, 19.5 µm, and 23.1 µm, respectively. Jian Gao's experimental result is approximately 12.5 µm, which is in good agreement with the predicted results at an Sr of 14.95 and ε of 0.60 (Figure 6b).

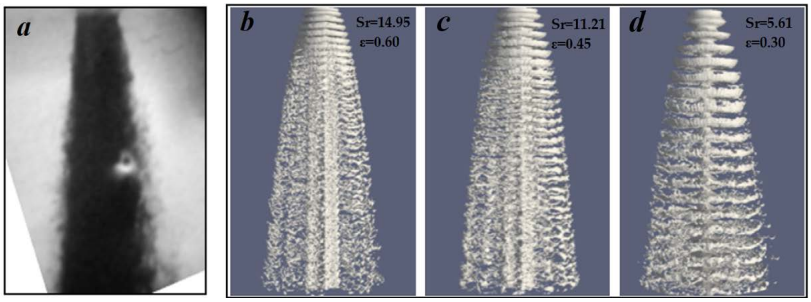

Figure 6. Shape of sprays obtained by Blessing et al. [46] and the simulation results. (**a**) Experimental image. Injection pressure P_{inj} = 80 MPa, i.e., injection spray velocity $U_{inj,l} \approx$ 336 m/s, ambient air pressure and temperature P_g = 0.1 MPa and T_g = 298.15 K, nozzle diameter D = 0.2 mm [46]; (**b**) Sr = 14.95, ε = 0.60; (**c**) Sr = 11.21, ε = 0.45; (**d**) Sr = 5.61, ε = 0.30.

A detailed view of the liquid–gas interface is shown in Figure 7. Surface waves are generated from the nozzle exit. Moving towards the downstream direction, the amplitude increases, and the surface waves break up into droplets. The wavelength of the surface wave becomes small with the increase in the disturbance frequency, and this phenomenon results in a difference in the droplet distribution. Figure 8 shows the distribution plot of the droplet size for the three cases. Droplet formation from wave sheets is observed. As the disturbance frequency increases, the wavelength and thickness of the wave sheet decrease, and the wave easily breaks up into droplets. The quantity of droplets increases, whereas the droplet size decreases with the increase in the disturbance frequency.

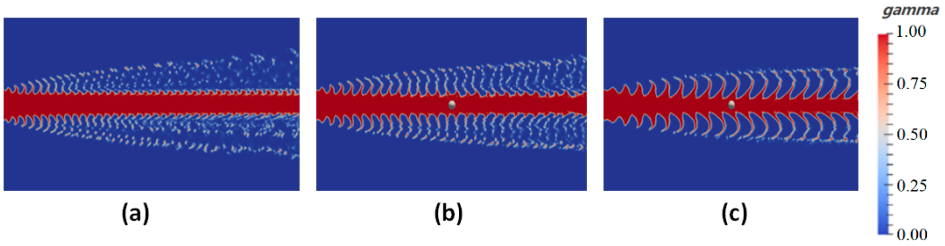

Figure 7. Contour of the liquid volume fraction for (**a**) Sr = 14.95 and ε = 0.61, (**b**) Sr = 11.21 and ε = 0.45, and (**c**) Sr = 5.61 and ε = 0.30.

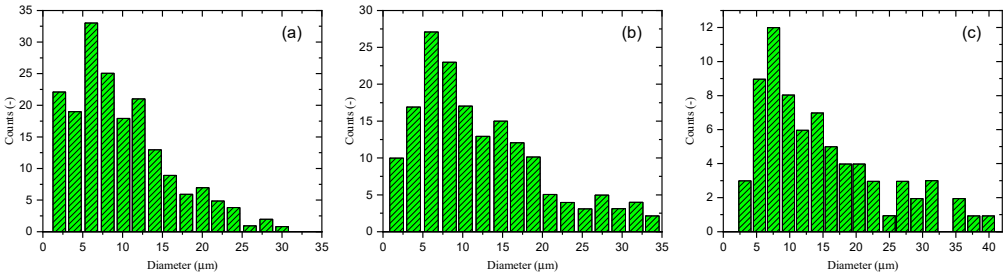

Figure 8. Droplet size distribution for (**a**) Sr = 14.95 and ε = 0.61, (**b**) Sr = 11.21 and ε = 0.45, and (**c**) Sr = 5.61 and ε = 0.30.

4.2. Ligament Formation from the Surface Wave

In this section, the breakup of the surface wave and ligament formation are analyzed with the results of the case where ε = 0.45 and f = 5000 kHz. Figure 9 shows the liquid surface shape for the chosen case. The liquid jet is disturbed by the radial velocity, such that surface waves occur from the liquid core, and the amplitude of the surface wave grows over time. The outer flow velocity is lower than the liquid core axial velocity due to the viscous stress on the liquid–gas interface, the crest of the surface waves is sheared by the aerodynamic force, and the strong shear deforms the surface wave. Therefore, umbrella-shaped crests are created. Finally, the most sheared part breaks up, and ligaments are formed from the edges of the crests. Ligament breakup is attributed to aerodynamic interaction, and satellite droplets are simultaneously created.

Figure 10 shows the time sequence of ligament formation from the edges of the crests. The blue arrow indicates an example of crest development and ligament breakup. Under the strong shear of aerodynamic force, a flat liquid sheet forms at the edges of the crest. Over time, the central part of the flat liquid sheet becomes thin because the rim is rounder and thicker than the central part because of surface tension. Flow shear results in the creation of a hole in the central region of the flat liquid sheet, and a doughnut-like shape is formed. The hole grows rapidly because of the contracting motion induced by surface tension. Finally, a ligament is produced at the edge of the crest.

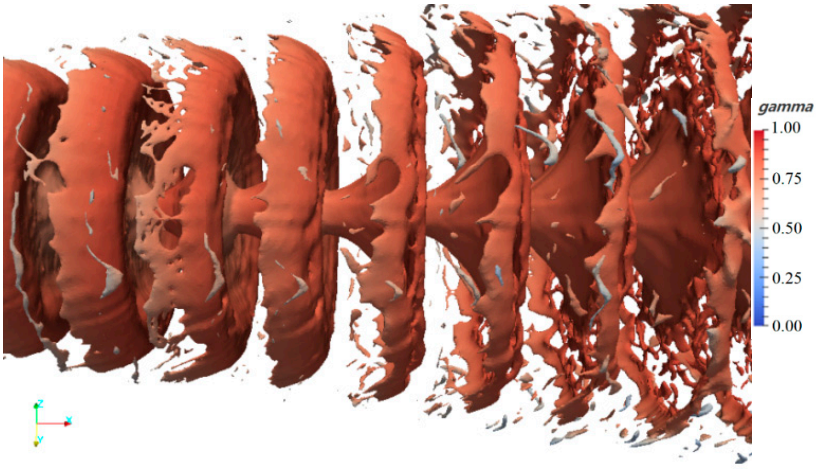

Figure 9. Liquid surface shape for a case where ε = 0.45 and f = 5000 kHz (Sr = 9.35).

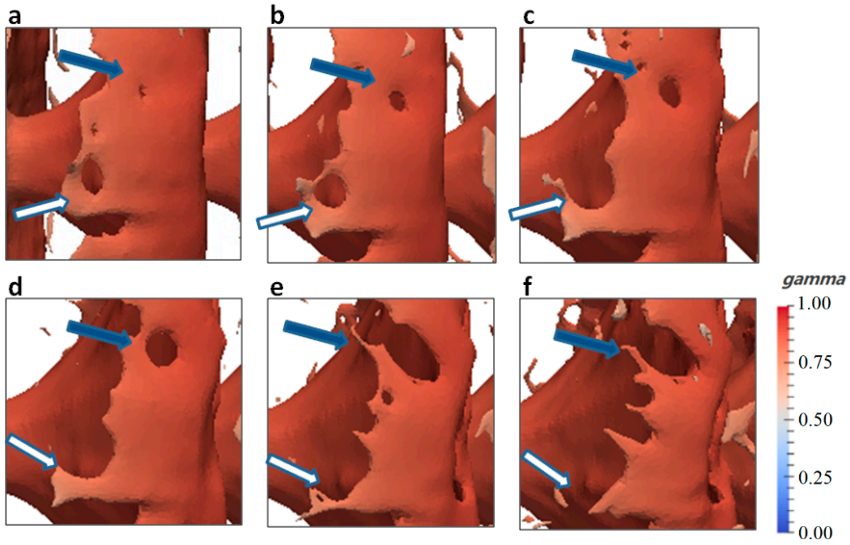

Figure 10. (**a**–**f**) Ligament formation from the liquid core (case ε = 0.45 and f = 5000 kHz (Sr = 9.35)). The results are presented with a time step difference (T) of 1×10^{-7} s.

Figure 11 shows the ligament formation process on a selected cross-section. The fluctuation on the windward side of the surface wave and the process of ligament formation can be observed. On the windward side of the surface wave, the fluctuation is mainly generated by aerodynamic force. Instability waves on the liquid surface propagate from the liquid core to the rim of the disc sheet, and the wave amplitude grows and results in ligament formation.

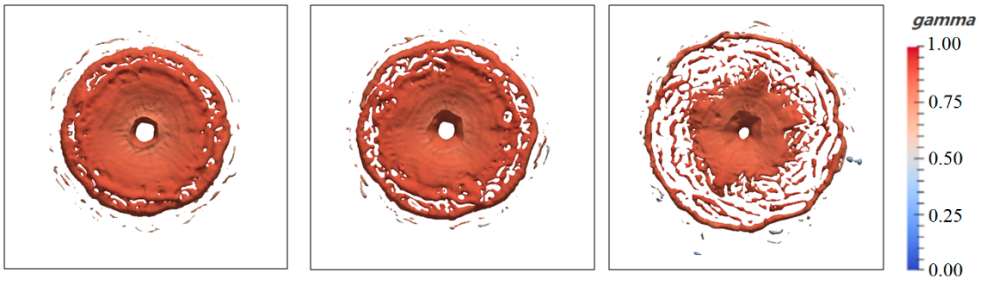

Figure 11. Ligament formation process from a visual angle on a select cross-section (case ε = 0.45 and f = 5000 kHz (Sr = 9.35)). The results are presented with a time step difference (T) of 1×10^{-7} s.

4.3. Characteristics of the Surface Wave

4.3.1. Analysis of Surface Wave Characteristics for Different Disturbance Frequencies

The simulation results of the liquid volume fraction for the conditions f = 3000 kHz to 9000 kHz and ε = 0.45 are presented in Figure 12. The sinusoidal radial velocity at the nozzle exit creates surface waves along the axis of the liquid jet. As the perturbation of surface waves grows along the flow direction, the thickness of the radial liquid sheet decreases as it is sheared, and surface tension breaks up the liquid sheet into ligaments. This process is called primary breakup. After primary breakup, ligaments may break up into small droplets, and this process is called secondary breakup. In this section, the characteristics of the surface wave and primary breakup are analyzed.

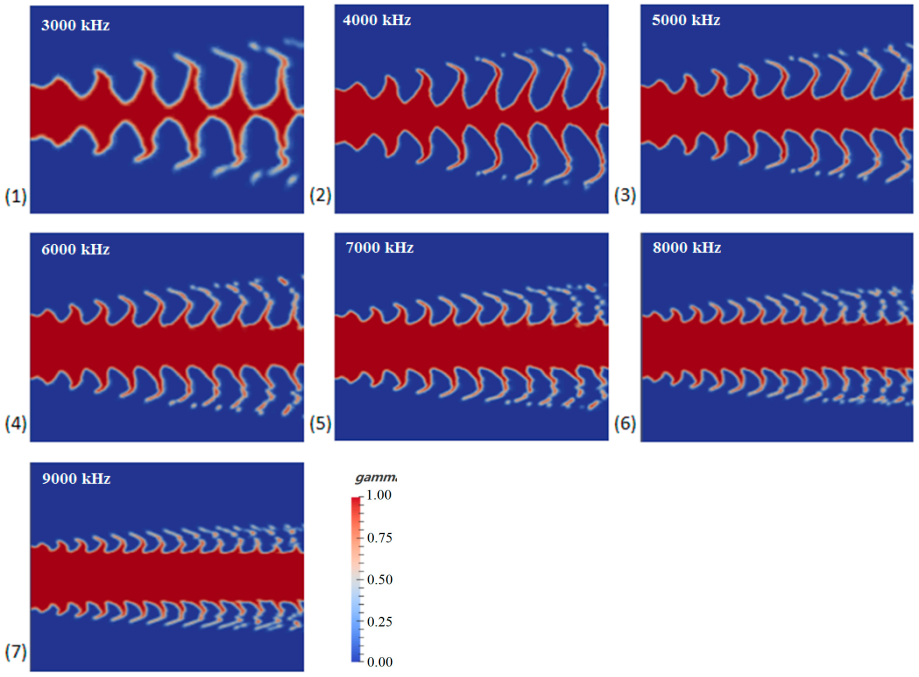

Figure 12. (**1**–**7**) Contour of the liquid volume fraction for f = 3000 kHz (Sr = 5.61) to 9000 kHz (Sr = 16.82) and ε = 0.45. The flow direction is from left to right.

To analyze the development of surface waves along the axis of the liquid jet, surface wave structures along the direction of jet development are counted and analyzed. The wave sequence number increases in degrees. Figure 13 shows the dimensionless amplitudes, η/R, of the surface waves corresponding to the different surface wave sequences at a disturbance amplitude of ε = 0.45 and the disturbance frequencies ranging from f = 3000 kHz to 9000 kHz. The surface wave sequence number closest to the nozzle exit is set to 1, and then the sequence number gradually increases along the downstream direction. For the seven disturbance frequencies, the amplitude of the surface waves increases nonlinearly along the flow direction. At the same surface wave amplitude, the higher the perturbation frequency the higher the number of surface waves. This indicates that increasing the perturbation frequency reduces the surface wave wavelength, which will facilitate the reduction of the droplet size. Figure 14 shows that the growth rate of the surface wave amplitude decreases with an increase in distance from the nozzle exit. The decay of the growth rate should be related to the viscous dissipation of the fluid.

To investigate the radial kinetic energy of surface waves, the radial kinetic energy of a surface wave can be estimated as

$$E = \frac{1}{2}\rho_l \eta \bar{h} v^2 \tag{14}$$

where ρ_l is the liquid density, η is the amplitude of the surface wave, $\overline{h}$ is the mean thickness of the surface wave sheet, and v is the mean radial velocity of the surface wave. The kinetic energies of the surface waves at ε = 0.45 and different perturbation frequencies are presented in Figure 15. The radial kinetic energy of the surface waves decreases along the downstream direction and also with the increase of the disturbance frequency. As we all know, air resistance causes a reduction in the radial kinetic energy of surface waves.

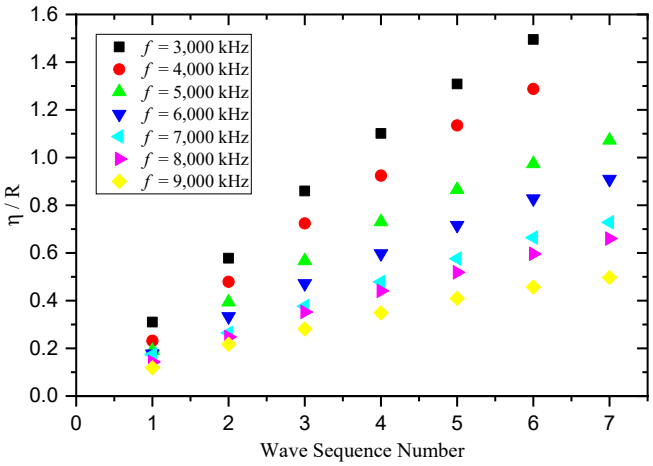

Figure 13. Amplitude of the surface waves at varying disturbance frequencies at ε = 0.45.

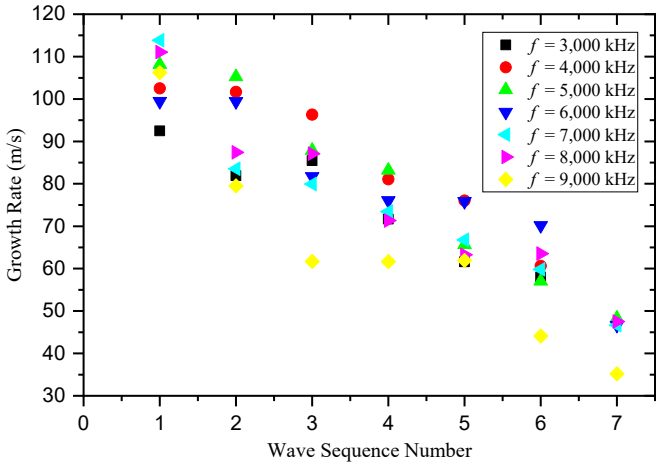

Figure 14. Growth rate of the surface wave amplitude for varying disturbance frequencies at ε = 0.45.

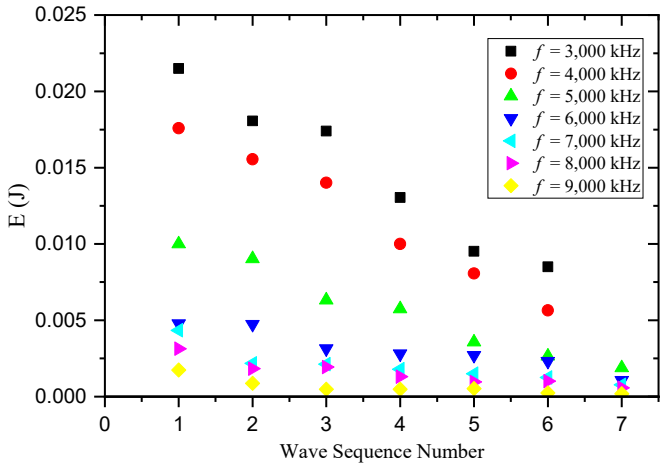

Figure 15. Radial Kinetic energy of surface waves with different disturbance frequencies at ε = 0.45.

4.3.2. Analysis of the Surface Wave Characteristics for Different Disturbance Amplitudes

As shown in Figure 16, the liquid volume fraction for the conditions of ε = 0.15, 0.30, 0.45, and 0.60 at f = 5000 kHz (Sr = 9.35). Notably, a change in disturbance amplitude has a negligible effect on the surface wavelength, but it evidently affects the surface wave amplitude.

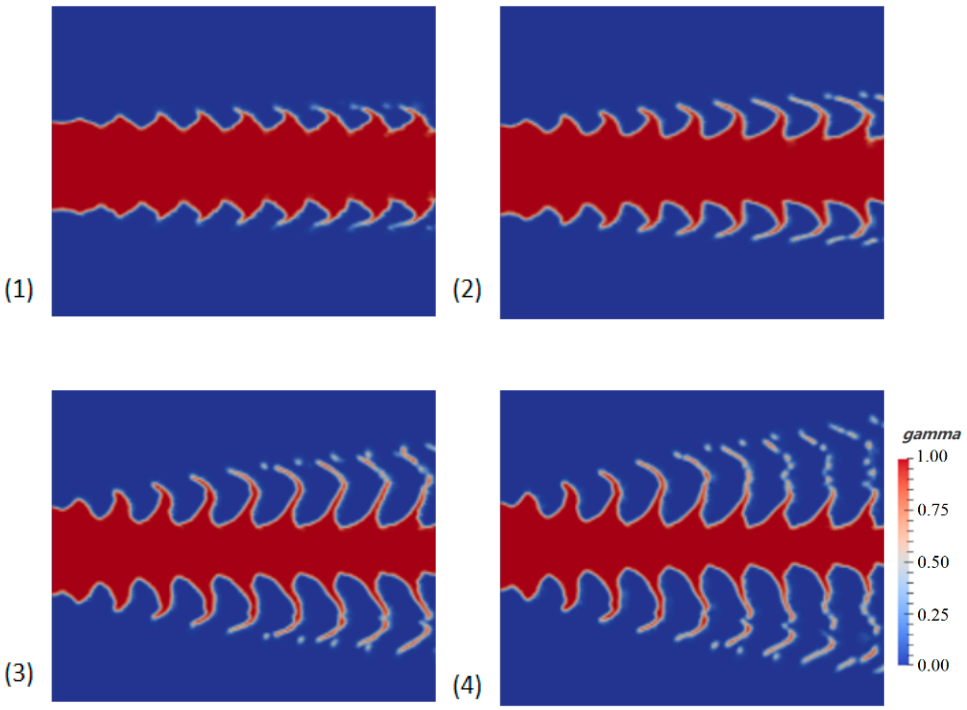

Figure 16. (**1**–**4**) Contour of the liquid volume fraction for f = 5000 kHz (Sr = 9.35) and ε = 0.15 to 0.60. The flow direction is from left to right.

The amplitude of surface waves and the growth rate of the surface wave amplitudes for varying disturbance amplitudes at Sr = 9.35 are presented in Figures 17 and 18, respectively. The results show that increasing the disturbance amplitude significantly increases the dimensionless surface wave amplitude of the jet (See Figure 17) and also increases the growth rate of the surface wave amplitude (See Figure 18).

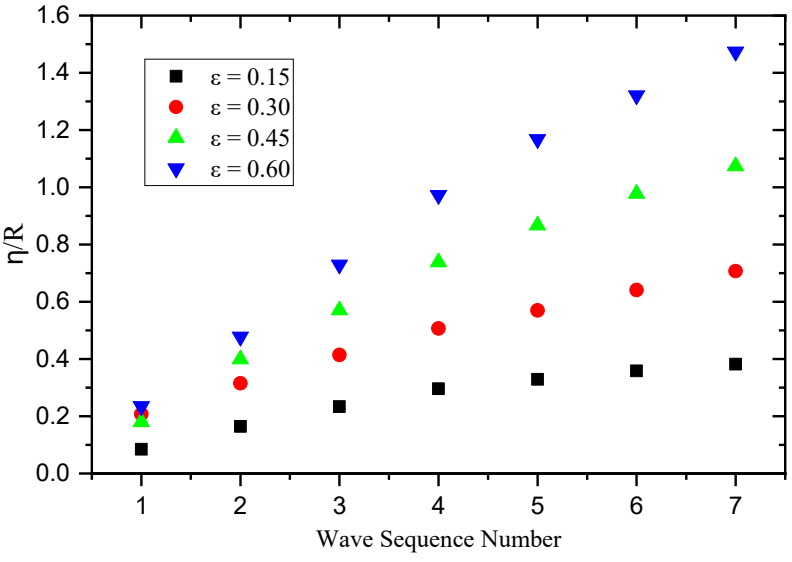

Figure 17. Amplitude of the surface waves for varying disturbance amplitudes at Sr = 9.35.

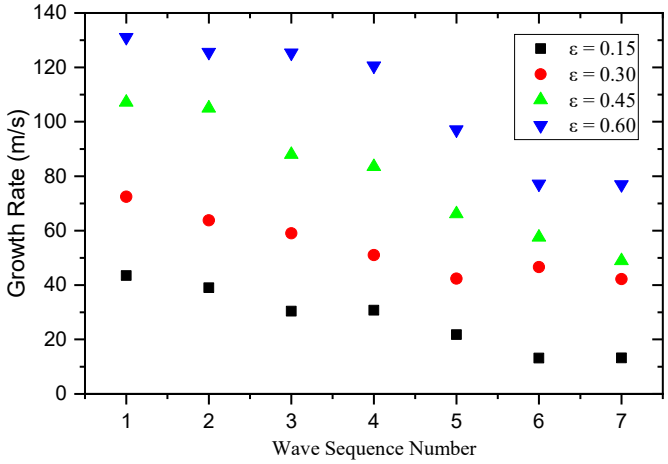

Figure 18. Growth rate of the surface wave amplitude for varying disturbance amplitudes at Sr = 9.35.

To demonstrate the effect of perturbation amplitude on radial kinetic energy of surface waves, the radial kinetic energies of different surface wave sequences at Sr = 9.35 are calculated (See Figure 19). The larger disturbance amplitude promotes radial kinetic energy, which facilitates the fragmentation of liquid filaments and the formation of liquid droplets.

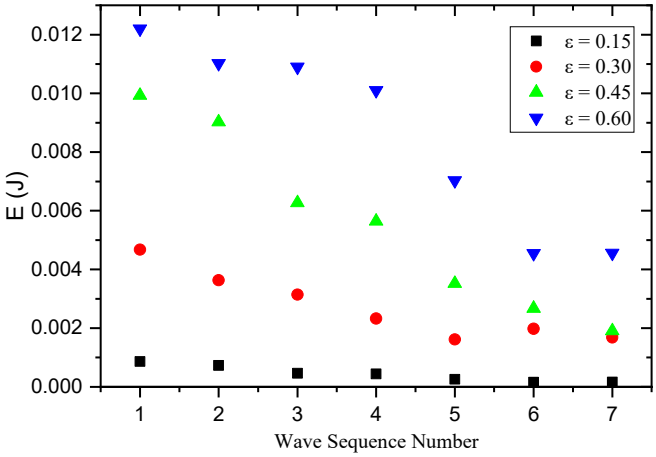

Figure 19. Energy of the surface wave sheet for varying disturbance amplitudes at Sr = 9.35.

4.4. Length and Time Scales of Liquid Jet Primary Breakup

For a disturbed liquid jet, ligament formation initially occurs from the edge of the surface wave sheet. The breakup of the surface wave sheet is considered the liquid jet primary breakup process. The length scale of primary breakup is determined by the size of the ligament formed from the surface wave sheet. The breakup of the surface wave sheet is affected by factors such as the radial velocity of the liquid sheet, viscous force, surface tension, and liquid gas density [53,54]. For the scaling analysis, the following set of dimensionless parameters is derived:

$$We = \frac{\rho_l U^2 h}{\sigma}; \quad Re = \frac{\rho_l U h}{\mu}; \quad Q = \frac{\rho_g}{\rho_l} \tag{15}$$

These parameters affect liquid sheet disintegration because, under different flow conditions, the liquid sheet exhibits different appearances with the change in the mechanisms that govern the liquid sheet.

To characterize the effect of surface tension, we identify a characteristic length [35] as

$$b = \frac{\sigma}{\rho_g U_{local}^2} \tag{16}$$

We assume that the size of the ligament formed from the liquid sheet is proportionate to the wavelength of the liquid sheet instability wave, whereas the latter is proportionate to the characteristic length (b). Therefore, the ligament diameter d is linear with b. We can characterize the breakup mode of the liquid sheet based on the ratio of b to the mean thickness of the surface wave sheet h:

$$\frac{b}{h} = \frac{\sigma}{\rho_g U_{local}^2 h} = \frac{\sigma}{\rho_l U_{local}^2 h}\frac{\rho_l}{\rho_g} = \frac{We}{Q} \tag{17}$$

When We > Q, the ligament diameter is larger than the liquid sheet thickness. The surface tension is the driving force for the breakup of the liquid sheet, and it shows a Rayleigh-type mechanism. When We < Q, the liquid sheet breakup is in atomization mode, and the sizes of the drops formed from the liquid sheet are significantly smaller than the sheet thickness.

Under the flow conditions in this paper, the local liquid Weber number We = 0.001 to 0.003, whereas the gas–liquid density ratio Q = 0.0015, both of which are in the same order of magnitude. The ligament diameter is in the same order of magnitude as the liquid sheet thickness. According to the regulation of the liquid sheet breakup mechanism, the breakup of liquid sheets in the present paper occurs in the first wind-induced regime [55]. The liquid sheet breakup occurs because of the relative motion between the liquid sheet and the gas, and as a result, the effect of surface tension is enhanced. The change in surface curvature results in an uneven static pressure distribution inside the liquid sheet. Therefore, the pressure gradient accelerates the breakup of the liquid sheet. Aerodynamics, pressure pulsation, and surface tension are the factors that jointly result in the breakup of the liquid sheet.

Equation (10) and the relations of the ligament diameter d and the characteristic length b indicate that the following formula can be derived:

$$d \propto b \propto h\frac{We}{Q} \tag{18}$$

The ligament diameter of the primary breakup is positively correlated with the local Weber number and the thickness of the liquid sheet, whereas the thickness of the liquid sheet is positively correlated with the wavelength of the surface wave. Figure 20 shows the plots of the primary breakup ligament diameter variation with the surface wavelength for different disturbance amplitudes (ε = 0.30, 0.45, and 0.60). A detailed view of the contour of the liquid volume fraction and the ligament formation features on a selected cross-section is shown in Figure 21. Figure 20 indicates that the ligament diameter of the primary breakup increases with an increase in the surface wavelength. From a detailed view of Figure 21, the wavelength of the surface wave and the thickness of the radial liquid sheet are reduced with an increase in disturbance frequency, a condition that reduces the primary breakup ligament diameter.

We also investigated the relationship between the disturbance amplitude and the primary breakup ligament diameter, as shown in Figure 22. For cases with the same disturbance frequency, the ligament diameter decreases as the disturbance amplitude increases. In this section, we define the Weber number as the ratio of the surface tension to the inertial force. This ratio varies inversely with the radial velocity squared. As the disturbance amplitude increases, the Weber number of the radial liquid sheet decreases and thus causes the inertial force to become the primary factor against surface tension. The inertial force promotes the breakup of the radial liquid sheet and decreases the length scale of the primary breakup. From another perspective, the increase in disturbance amplitude increases the radial kinetic energy of the liquid sheet and thus promotes radial expansion and reduces the thickness of the liquid sheet. This condition can also contribute to the decrease in the primary breakup ligament diameter.

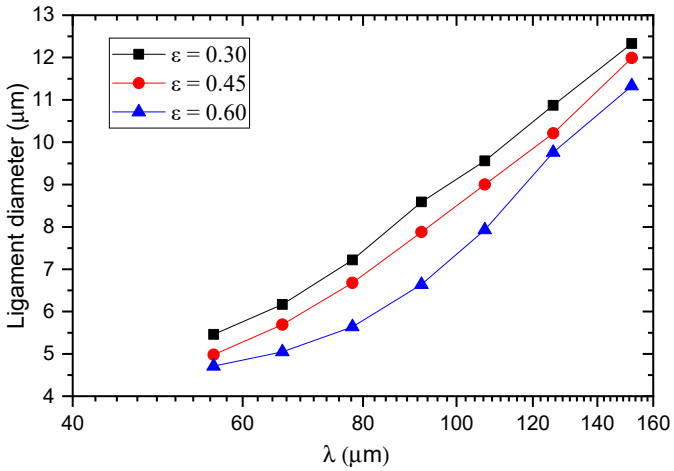

Figure 20. Plots of primary breakup ligament diameter variation with the surface wavelength for different disturbance amplitudes.

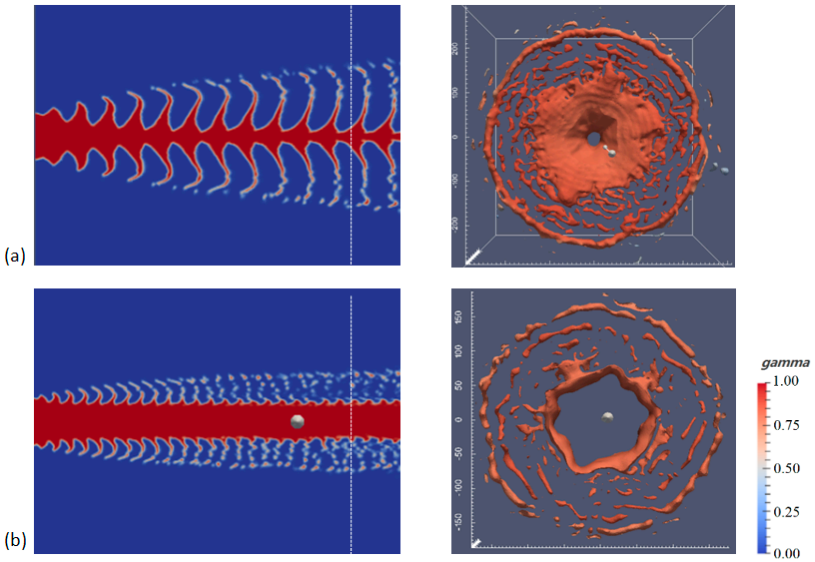

Figure 21. Contour plot of the volume fraction and contour of liquid volume fraction, as well as ligament formation features, on a selected cross-section taken from simulations with (**a**) $\varepsilon = 0.45$ and $f = 4000$ Hz ($Sr = 7.48$) and (**b**) $\varepsilon = 0.45$ and $f = 8000$ Hz ($Sr = 0.15$).

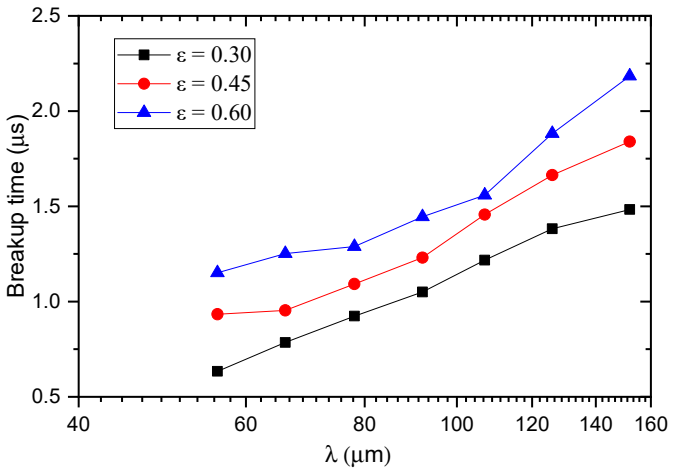

Figure 22. Plots of primary breakup time variation with the surface wavelength for different disturbance amplitudes.

We define the primary breakup time t_b as the period from the start of injection to the time when ligament formation first occurs. Figure 22 presents the plot of primary breakup time variation with an increase in surface wavelength for different disturbance amplitudes (ε = 0.30, 0.45, and 0.60). Figure 22 shows that for the cases of ε = 0.30, 0.45, and 0.60, the breakup time increases as the surface wavelength increases. This condition can be attributed to the increase in surface wavelength, which in turn increases the thickness of the liquid sheet. This condition is unfavorable for the breakup of the liquid sheet and thus increases the primary breakup time.

From another perspective, as the disturbance amplitude increases while the surface wavelengths remain the same, the primary breakup time decreases. This trend indicates that the increasing disturbance amplitude promotes the atomization of a disturbed liquid jet.

5. Conclusions

In this study, a CFD methodology that combines the LES model with a VOF technique for free surface capture was successfully applied to simulate the primary breakup of a high-speed diesel jet. By simplifying inner-nozzle turbulence and cavitation as the sinusoidal radial velocity, we computed the primary atomization of a disturbed liquid jet. We mainly focused on the atomization characteristics and physical mechanism of primary breakup. The following results were obtained:

The variation in the disturbance amplitude and frequency facilitates the formation of a variety of liquid structures, such as waves, upstream/downstream-directed bells, and droplet chains.

Ligament formation occurs from the edge of the surface wave crest. As the liquid jet is disturbed by the radial velocity, surface waves occur from the liquid core, and umbrella-shaped crests are created. We note from the simulations that the amplitude of surface waves increases along the flow direction, and the growth rate of the amplitude decreases with distance from the nozzle exit. The variation in disturbance frequency evidently affects the surface wave amplitude. Increasing the disturbance frequency reduces the growth rate of the surface waves of the liquid jet and thus decreases the surface wave amplitude. With an increase in disturbance amplitude, the amplitude of surface waves evidently increases.

The ligament diameter of primary breakup is positively correlated with the local Weber number and the thickness of the radial liquid sheet. Therefore, as the disturbance frequency and amplitude increase, the thickness and Weber number of the radial liquid sheet decrease, and this causes the ligament diameter of the primary breakup to become small. The time scale of the liquid jet primary breakup decreases as the disturbance amplitude increases, which indicates that an increase in the disturbance amplitude promotes the atomization of a disturbed liquid jet.

Author Contributions: Conceptualization, Z.L. (Zhenming Liu), Z.L. (Ziming Li) and J.W.; methodology, Z.L. (Zhenming Liu), Z.L. (Ziming Li) and J.L.; software, J.L.; validation, Z.L. (Zhenming Liu) and Z.L. (Ziming Li); formal analysis, J.L.; resources, Y.Y.; writing—original draft preparation, Z.L. (Zhenming Liu) and Z.L. (Ziming Li); writing—review and editing, Z.L. (Zhenming Liu), Z.L. (Ziming Li), J.W., J.D. and Y.Y.; supervision, Z.L. (Zhenming Liu); funding acquisition, Z.L. (Zhenming Liu). All authors have read and agreed to the published version of the manuscript.

Funding: This research was funded by the National Natural Science Foundation of China, grant no. 51879269.

Institutional Review Board Statement: Not applicable.

Informed Consent Statement: Not applicable.

Data Availability Statement: Some data, models, or code that support the findings of this study are available from the corresponding author upon reasonable request.

Conflicts of Interest: The authors declare no conflict of interest.

Nomenclature

b	Characteristic length (m)
d	Liquid ligament diameter (m)
D	Nozzle diameter (m)
E	Kinetic energy (J)
f	Disturbance frequency (1/s)
F_s	Surface tension force (N)
h	Mean thickness of the surface wave sheet (m)
k	Turbulent kinetic energy (m^2/s^2)
$\vec{n}$	Normal vector
p	Pressure (Pa)
t_b	Primary breakup time (s)
t	Time (s)
T	Temperature (K)
$\overline{u}$	Velocity (m/s)
U	Axial velocity of liquid jet (m/s)
x, y, z	Coordinate (m)
ρ	Density (kg/m^3)
μ	Dynamic viscosity (Pa·s)
τ_{ij}	Subgrid scale (SGS) stress (m^2/s^2)
v_t	SGS viscosity (N/m^2)
$\overline{S}_{ij}$	Mean strain rate tensor (s^{-1})
γ	Volume fraction
σ	Surface tension of the liquid (N/m)
κ	Curvature (1/m)
η	Amplitude (m)
ε	Disturbance amplitude ratio
Sr	Strouhal number
Re	Reynolds number
Q	Liquid–gas density ratio
We	Weber number
Subscripts	
Axial	Axial direction
cav	Cavitation
g	Gas
inj	Injection
i, j, k	Unit vectors in the x-, y-, and z-directions
l	Liquid
local	Local
max	Maximum
rad	Radial direction

References

1. Lin, S.P. *Breakup of Liquid Sheets and Jets*; Cambridge University Press: New York, NY, USA, 2003.
2. Shinjo, J. Recent advances in computational modeling of primary atomization of liquid fuel sprays. *Energies* **2018**, *11*, 2971. [CrossRef]
3. Chen, Y.; Chen, S.; Chen, W.; Hu, J.; Jiang, J. An Atomization Model of Air Spraying Using the Volume-of-Fluid Method and Large Eddy Simulation. *Coatings* **2021**, *11*, 1400. [CrossRef]
4. Stahl, M.; Damaschke, N.; Tropea, C. Experimental investigation of turbulence and cavitation inside a pressure atomizer and optical characterization of the generated spray. In Proceedings of the 10th ICLASS Conference, Kyoto, Japan, 27 August–1 September 2006.
5. Bagué, A.; Fuster, D.; Popinet, S. Instability growth rate of two-phase mixing layers from a linear eigenvalue problem and an initial-value problem. *Phys. Fluids* **2010**, *22*, 092104. [CrossRef]
6. He, Z.; Guo, G.; Tao, X.; Zhong, W.; Leng, X.; Wang, Q. Study of the effect of nozzle hole shape on internal flow and spray characteristics. *Int. Commun. Heat Mass* **2016**, *71*, 1–8. [CrossRef]
7. Suh, H.K.; Lee, C.S. Effect of cavitation in nozzle orifice on the diesel fuel atomization characteristics. *Int. J. Heat Fluid Flow* **2008**, *29*, 1001–1009. [CrossRef]

8. Badock, C.; Wirth, R.; Fath, A. Investigation of cavitation in real size diesel injection nozzles. *Int. J. Heat Fluid Flow* **1999**, *20*, 538–544. [CrossRef]
9. Shinjo, J.; Umemura, A. Simulation of liquid jet primary breakup: Dynamics of ligament and droplet formation. *Int. J. Multiph. Flow* **2010**, *36*, 513–532. [CrossRef]
10. Shinjo, J.; Umemura, A. Surface instability and primary atomization characteristics of straight liquid jet sprays. *Int. J. Multiph. Flow* **2011**, *37*, 1294–1304. [CrossRef]
11. He, Z.; Zhou, H.; Duan, L.; Xu, M.; Chen, Z.; Cao, T. Effects of nozzle geometries and needle lift on steadier string cavitation and larger spray angle in common rail diesel injector. *Int. J. Engine Res.* **2021**, *22*, 2673–2688. [CrossRef]
12. Reitz, R.D.; Bracco, F.V. Mechanism of atomization of a liquid jet. *Phys. Fluids* **1982**, *25*, 1730. [CrossRef]
13. Lin, S.P.; Reitz, R.D. Drop and spray formation from a liquid jet. *Annu. Rev. Fluid Mech.* **1998**, *30*, 85–105. [CrossRef]
14. Zhao, W.; Yan, J.; Gao, S.; Lee, T.H.; Li, X. Effects of fuel properties and aerodynamic breakup on spray under flash boiling conditions. *Appl. Therm. Eng.* **2022**, *200*, 117646. [CrossRef]
15. Schweitzer, P.H. Mechanism of disintegration of liquid jets. *J. Appl. Phys.* **1937**, *8*, 513–521. [CrossRef]
16. Bergwerk, W. Flow pattern in diesel nozzle spray holes. *Proc. Inst. Mech. Eng.* **1959**, *173*, 655–660. [CrossRef]
17. Chaves, H.; Knapp, M.; Kubitzek, A. Experimental study of cavitation in the nozzle hole of diesel injectors using transparent nozzles. *SAE Trans.* **1995**, *104*, 645–657.
18. Soteriou, C. Direct Injection Diesel Spray and the Effect of Cavitation and Hydraulic Flip or Atomization. *SAE Trans.* **1995**, *104*, 128–153.
19. Wei, Y.; Fan, L.; Zhang, H.; Gu, Y.; Deng, Y.; Leng, X.; Fei, H.; He, Z. Experimental investigations into the effects of string cavitation on diesel nozzle internal flow and near field spray dynamics under different injection control strategies. *Fuel* **2022**, *309*, 122021. [CrossRef]
20. McCormack, P.D.; Crane, L.; Birch, S. An experimental and theoretical analysis of cylindrical liquid jets subjected to vibration. *Br. J. Appl. Phys.* **1965**, *16*, 395. [CrossRef]
21. Chaves, H.; Obermeier, F.; Seidel, T. Fundamental investigation of the disintegration of a sinusoidally forced liquid jet. In Proceedings of the ICLASS-2000, Tsukuba, Japan, 13–15 December 2000; pp. 1018–1025.
22. Geschner, F.; Obermier, G.; Chaves, H. Investigation of different phenomena of the disintegration of a sinusoidally forced liquid jet. In Proceedings of the Seventeenth Annual Conference on Liquid Atomization and Spray Systems, Zurich, Switzerland, 2–6 September 2001.
23. Srinivasan, V.; Salazar, A.J.; Saito, K. Modeling the disintegration of modulated liquid jets using volume-of-fluid (VOF) methodology. *Appl. Math. Model.* **2011**, *35*, 3710–3730. [CrossRef]
24. Srinivasan, V.; Salazar, A.J.; Saito, K. Numerical simulation of the disintegration of forced liquid jets using volume-of-fluid method. *Int. J. Comput. Fluid Dyn.* **2010**, *24*, 317–333. [CrossRef]
25. Hwang, H.; Kim, D.; Moin, P. Atomization of the optimally disturbed liquid jet. *Bull. Am. Phys. Soc.* **2021**, *66*, 17.
26. Zhou, C.; Zou, J.; Zhang, Y. Effect of Streamwise Perturbation Frequency on Formation Mechanism of Ligament and Droplet in Liquid Circular Jet. *Aerospace* **2022**, *9*, 191. [CrossRef]
27. Linne, M.; Paciaroni, M.; Hall, T. Ballistic imaging of the near field in a diesel spray. *Exp. Fluids* **2006**, *40*, 836–846. [CrossRef]
28. Blaisot, J.B.; Yon, J. Droplet size and morphology characterization for dense sprays by image processing: Application to the Diesel spray. *Exp. Fluids* **2005**, *39*, 977–994. [CrossRef]
29. Wang, Y.; Liu, X.; Im, K.S. Ultrafast X-ray study of dense-liquid-jet flow dynamics using structure-tracking velocimetry. *Nat. Phys.* **2008**, *4*, 305–309. [CrossRef]
30. Salvador, F.J.; Gimeno, J.; De La Morena, J.; González-Montero, L.A. Experimental analysis of the injection pressure effect on the near-field structure of liquid fuel sprays. *Fuel* **2021**, *292*, 120296. [CrossRef]
31. Payri, R.; Gimeno, J.; Martí-Aldaraví, P.; Martínez, M. Transient nozzle flow analysis and near field characterization of gasoline direct fuel injector using Large Eddy Simulation. *Int. J. Multiph. Flow* **2022**, *148*, 103920. [CrossRef]
32. Mukundan, A.A.; Ménard, T.; De Motta, J.C.B.; Berlemont, A. Detailed numerical simulations of primary atomization of airblasted liquid sheet. *Int. J. Multiph. Flow* **2022**, *147*, 103848. [CrossRef]
33. Ménard, T.; Tanguy, S.; Berlemont, A. Coupling level set/VOF/ghost fluid methods: Validation and application to 3D simulation of the primary break-up of a liquid jet. *Int. J. Multiph. Flow* **2007**, *33*, 510–524. [CrossRef]
34. Desjardins, O.; Moureau, V.; Pitsch, H. An accurate conservative level set/ghost fluid method for simulating turbulent atomization. *J. Comput. Phys.* **2008**, *227*, 8395–8416. [CrossRef]
35. De Villiers, E.; Gosman, A.D.; Weller, H.G. Large eddy simulation of primary diesel spray atomization. *SAE Trans.* **2004**, *113*, 193–206.
36. Pai, M.G.; Desjardins, O.; Pitsch, H. Detailed simulations of primary breakup of turbulent liquid jets in crossflow. *Cent. Turbul. Res. Annu. Res. Briefs* **2008**, *34*, 451–466.
37. Herrmann, M. A balanced force refined level set grid method for two-phase flows on unstructured flow solver grids. *J. Comput. Phys.* **2008**, *227*, 2674–2706. [CrossRef]
38. Herrmann, M. Detailed numerical simulations of the primary breakup of turbulent liquid jets. In Proceedings of the 21st Annual Conference of ILASS Americas, Orlando, FL, USA, 18–21 May 2008; pp. 1–17.

39. Herrmann, M. The impact of density ratio on the primary atomization of a turbulent liquid jet in crossflow. *Bull. Am. Phys. Soc.* **2009**, *54*, 191–205.
40. Liu, K.; Huck, P.D.; Aliseda, A.; Balachandar, S. Investigation of turbulent inflow specification in Euler–Lagrange simulations of mid-field spray. *Phys. Fluids* **2021**, *33*, 033313. [CrossRef]
41. Daskiran, C.; Xue, X.; Cui, F.; Katz, J.; Boufadel, M.C. Impact of a jet orifice on the hydrodynamics and the oil droplet size distribution. *Int. J. Multiph. Flow* **2022**, *147*, 103921. [CrossRef]
42. Apte, S.V.; Gorokhovski, M.; Moin, P. LES of atomizing spray with stochastic modeling of secondary breakup. *Int. J. Multiph. Flow* **2003**, *29*, 1503–1522. [CrossRef]
43. Ubbink, O. Numerical Prediction of Two Fluid Systems with Sharp Interfaces. Ph.D. Thesis, University of London, London, UK, 1997.
44. Brackbill, J.U.; Kothe, D.B.; Zemach, C. A continuum method for modeling surface tension. *J. Comput. Phys.* **1992**, *100*, 335–354. [CrossRef]
45. Martínez, J.; Piscaglia, F.; Montorfano, A.; Onorati, A.; Aithal, S.M. Influence of momentum interpolation methods on the accuracy and convergence of pressure–velocity coupling algorithms in OpenFOAM®. *J. Comput. Appl. Math.* **2017**, *309*, 654–673. [CrossRef]
46. Blessing, M.; König, G.; Krüger, C. Analysis of flow and cavitation phenomena in Diesel injection nozzles and its effects on spray and mixture formation. *SAE Trans.* **2003**, *112*, 1694–1706.
47. Ghiji, M.; Goldsworthy, L.; Brandner, P.A.; Garaniya, V.; Hield, P. Analysis of diesel spray dynamics using a compressible Eulerian/VOF/LES model and microscopic shadowgraphy. *Fuel* **2017**, *188*, 352–366. [CrossRef]
48. Martinez, L.; Benkenida, A.; Cuenot, B. A model for the injection boundary conditions in the context of 3D simulation of diesel spray: Methodology and validation. *Fuel* **2010**, *89*, 219–228. [CrossRef]
49. Huh, K.Y.; Lee, E.; Koo, J. Diesel Spray Atomization Model Considering Nozzle Exit Turbulence Conditions. *At. Sprays* **1998**, *8*, 453–469. [CrossRef]
50. Baumgarten, C.; Stegemann, J.; Merker, G.P. A New Model for Cavitation Induced Primary Break-up of Diesel Sprays. In Proceedings of the ILASS-Europe 2002, Zaragoza, Spain, 9 September–9 November 2002.
51. Sarre, C.; Kong, S.C.; Reitz, R.D. Modeling the effects of injector nozzle geometry on diesel sprays. *SAE Pap.* **1999**, *108*, 1375–1388.
52. Gao, J.; Park, S.W.; Wang, Y.; Reitz, R.D.; Moon, S.; Nishida, K. Simulation and analysis of group-hole nozzle sprays using a gas jet superposition model. *Fuel* **2010**, *89*, 3758–3772. [CrossRef]
53. Lin, S.P.; Kang, D.J. Atomization of a liquid jet. *Phys. Fluids* **1987**, *30*, 2000. [CrossRef]
54. Lin, S.P.; Lian, Z.W. Mechanisms of the breakup of liquid jets. *AIAA J.* **1990**, *28*, 120–126. [CrossRef]
55. Ranz, W.E. *On Sprays and Spraying*; College of Engineering and Architecture: Washindgton, DC, USA, 1959.